INORGANIC CHEMISTRY
FRONTIERS

RESEARCH ARTICLE

View Article Online
View Journal | View Issue

Cite this: *Inorg. Chem. Front.*, 2026, **13**, 1080

Strain-controlled decomposition efficiency of $LaCoO_3$ perovskite epitaxial thin films

Jie Tu, †[a] Siyuan Du,†[a] Hangren Li,†[a,b] Jing Xia,*[c] Longyuan Shi,[a] Jianjun Tian [a] and Linxing Zhang *[a,d]

Strain engineering has emerged as a powerful strategy for optimizing the material structure and enhancing performance across a wide range of applications. Herein, we report the deployment of substrate-imposed strain to govern the dissolution kinetics of an epitaxial sacrificial layer. The epitaxial $LaCoO_3$ (LCO) has been employed as a sacrificial layer: a lattice-matched and environmentally benign perovskite for releasing freestanding oxide membranes. Intriguingly, the decomposition efficiency of LCO can be precisely controlled by the substrate strain, whether tensile or compressive, which can induce changes in chemical bonds and lattice distortion, thereby altering the reactivity of LCO with the decomposition solution. Under a tensile strain of 2.09% on $SrTiO_3$ substrate, the decomposition efficiency of LCO was accelerated by 66.7% compared with that on $LaAlO_3$ substrate with compressive strain. Synchrotron X-ray absorption spectroscopy, high-angle annular dark-field scanning transmission electron microscopy and semi-*in situ* optical absorption spectra reveal that tensile strain reduces La–O bond energy and enhances octahedral distortion, making the lattice more susceptible to collapse. Furthermore, freestanding $PbZrO_3$ films were fabricated using the LCO sacrificial layer, showing a ferroelectric-to-antiferroelectric transition. These findings underscore the potential of strain engineering in controlling material properties and fabrication processes, offering new strategies for developing flexible electronic devices.

Received 9th September 2025,
Accepted 11th November 2025

DOI: 10.1039/d5qi01871d

rsc.li/frontiers-inorganic

Introduction

With the development of miniaturization and flexibility of materials, the preparation and application of functional freestanding thin film materials have become research hotspots.[1,2] Among them, the effective integration of functional thin films with substrates of different properties is a crucial step in realizing high-performance devices. In the development of freestanding thin films, the selection of sacrificial layers in the chemical wet etching process is of significant importance.[3] Recently, numerous studies have been dedicated to exploring various materials suitable as sacrificial layers, such as ZnO,[4] $SrTiO_3$ (STO),[5] $La_{0.7}Sr_{0.3}MnO_3$ (LSMO),[6] $YBa_2Cu_3O_{7-x}$ (YBCO),[7] $SrRuO_3$ (SRO),[8] $SrCoO_{2.5}$ (SCO),[9] $SrVO_3$ (SVO),[10] $Sr_3Al_2O_6$ (SAO_C)[3] and $Sr_4Al_2O_7$ (SAO_T).[11] These materials have met some application requirements to a certain extent, but they also face many challenges. For instance, materials such as LSMO, STO, and SRO require stringent etching conditions and need to be etched with strongly corrosive or strongly oxidizing etchants. This not only increases the difficulty and danger of experimental operation but also may damage the target layer. Although SAO and SCO can be etched with water or weak acid solutions, they do not have a perovskite structure. Therefore, it is of great significance to develop a perovskite sacrificial layer that has good atomic matching, good controllability, high stability and is environmentally friendly.

Strain engineering plays a crucial role in optimizing material properties.[12–14] It can alter a variety of material characteristics and subsequently affect their performance in different application scenarios. Strain modulation has been widely utilized to enhance material performance.[15,16] For example, in semiconductor materials, the application of external strain can effectively regulate the band structure, thereby modifying the electron mobility and optical properties, which offers an important approach for improving the performance of semiconductor devices.[17] In piezoelectric materials, strain can adjust the polarization states, enhancing the piezoelectric response and enabling them to have greater utility in sensors and energy conversion devices.[18] For $LaCoO_3$ (LCO) perovskite films, strain modulation also has a non-negligible impact. On

[a]*Institute for Advanced Materials Technology, University of Science and Technology Beijing, Beijing 100083, China. E-mail: linxingzhang@ustb.edu.cn*
[b]*State Key Laboratory of New Ceramics and Fine Processing, School of Materials Science and Engineering, Tsinghua University, Beijing 100084, China*
[c]*Key Laboratory of Photochemical Conversion and Optoelectronic Materials, Technical Institute of Physics and Chemistry Chinese Academy of Sciences, Beijing, 100190, China. E-mail: xiajing@mail.ipc.ac.cn*
[d]*Institute of Solid State Chemistry, University of Science and Technology Beijing, Beijing 100083, China*
†These authors contributed equally to this work.

the one hand, strain can modify the lattice structure of LCO films, leading to changes in the lattice constant and influencing the lattice matching degree with other materials, which is essential for the fabrication and integration of heterostructures based on LCO films.[19–21] On the other hand, strain may also affect the internal charge distribution and chemical bonding state of LCO films, thus altering their physical properties, such as ferromagnetic properties.[22–26]

Here, we have discovered that substrate strain plays a crucial role in the decomposition process of the LCO sacrificial layer, significantly influencing its decomposition efficiencies on different substrates, such as STO and $LaAlO_3$ (LAO). The underlying cause is that substrate strain induces changes in the La–O bond characteristics, which in turn alter the reactivity of LCO with the decomposition solution. Specifically, tensile or compressive strain can modify bond lengths and angles, affecting the bond energy and making the material more or less susceptible to decomposition. In addition, we have found that LCO films can be decomposed by acetic acid (CH_3COOH), a relatively low corrosiveness decomposition solution, which renders the etching process safer, more environmentally friendly, and easier to operate. Moreover, LCO films have a perovskite structure, conferring a unique advantage in exfoliating perovskite functional thin films by achieving outstanding atomic matching. This phenomenon highlights the importance of strain in determining the decomposition behavior of LCO and provides a new research direction for an in-depth understanding of the etching mechanism of sacrificial layer materials.

Experimental details

The required amounts of $La(NO_3)_3{\cdot}6H_2O$ (Aladdin, 99.99%) and $C_4H_6CoO_4{\cdot}4H_2O$ (Macklin, 99.5%) were dissolved in 2-methoxyethanol (Aladdin, 99.5%). The mixture was heated at 75 °C with stirring for 2 h to form a red transparent precursor solution, which was then filtered at room temperature. The precursor was spin-coated onto STO or LAO substrates at 5000 rpm for 30 s, heated at 120 °C for 3 min to remove moisture, at 350 °C for 10 min to eliminate organics, and finally annealed at 650 °C for 30 min in a muffle furnace to obtain LCO films. The required amounts of $Pb(NO_2)_3$ (Aladdin, 99.999%) and $Zr(NO_3)_4{\cdot}5H_2O$ (Boer, 99.99%) were dissolved in 2-methoxyethanol (Aladdin, 99.5%). The mixture was heated at 75 °C with stirring for 2 h to form a colorless transparent precursor solution, which was then filtered at room temperature. The precursor was spin-coated onto LCO/STO or LCO/LAO substrates at 5000 rpm for 30 s, heated at 120 °C for 3 min to remove moisture, at 350 °C for 10 min to eliminate organics, and finally annealed at 750 °C for 30 min in a muffle furnace to obtain PZO films.

For the immersion decomposition process, LCO/STO or LCO/LAO samples were placed in a 10% CH_3COOH solution and the absorption spectrum was collected at the expected time intervals. For the directional electrodynamic decomposition process, a 304 stainless steel clip was used to grasp a corner of the PZO films. This clip was affixed to the anode of the current source. Subsequently, the cathode of the current source was then connected to the carbon rod, which was then immersed in an 10% CH_3COOH solution. An applied voltage of 10 V was used for PZO films. The LCO sacrificial layer will be decomposed. The structural, electrical, optical and more testing procedures are described in the Supplementary Information.

Results and discussion

In the case of LCO perovskite films, two distinct epitaxial growth modes are observed on the typical LAO and STO substrates. Theoretically, a 1 : 1 lattice matching relationship is anticipated between the LCO films and the substrates, given that both exhibit a perovskite structure. However, the actual lattice matching deviates from this ideal due to differences in lattice constants.[27] LAO has a lattice constant of 3.79 Å, which is smaller than that of LCO (3.82 Å), while STO has a lattice constant of 3.90 Å, which is larger than that of LCO. When considering the lattice mismatch, it is important to distinguish between the in-plane direction and the out-of-plane direction. In the in-plane direction, LCO films experience compressive strain when deposited on LAO substrates due to the smaller lattice constant of LAO, while they experience tensile strain when deposited on STO substrates due to the larger lattice constant of STO. This can be quantified using the lattice mismatch formula:

$$f = 1 - d_{\text{overlayer}}/d_{\text{substrate}}$$

The degree of mismatch is calculated to be −0.79% for LCO films on LAO substrates (the compressive strain along the in-plane direction) and 2.09% for LCO films on STO substrates (the tensile strain along the in-plane direction) (Fig. 1A and B). The strain situation is reversed along the out-of-plane direction. Specifically, LCO films experience tensile strain when deposited on LAO substrates and compressive strain when deposited on STO substrates.

The strain induced by lattice mismatch significantly impacts the lattice constants of LCO films. The X-ray diffraction (XRD) patterns in the large angle region (15°–55°) reveal the diffraction peaks of the (00L) planes for both the substrates and films (Fig. S1A). The one-to-one correspondence of the diffraction peaks confirms that the (001) plane of the films is parallel to that of the substrates. We determined the single-crystalline characteristics of the LCO films by comparing the rocking curves of the substrates and the films (Fig. S2).[28,29] It is worth noting that there are some diffraction peaks originating from the substrates with other wavelengths of X-rays, such as Cu K_β (Fig. S1B). The positions of the (002) diffraction peak of the films vary with the substrate type and film thickness, indicating the effects of substrate strain and the changes in lattice constants. Specifically, the (002) diffraction peak of the 60 nm LCO films on LAO substrates shifts to a lower angle

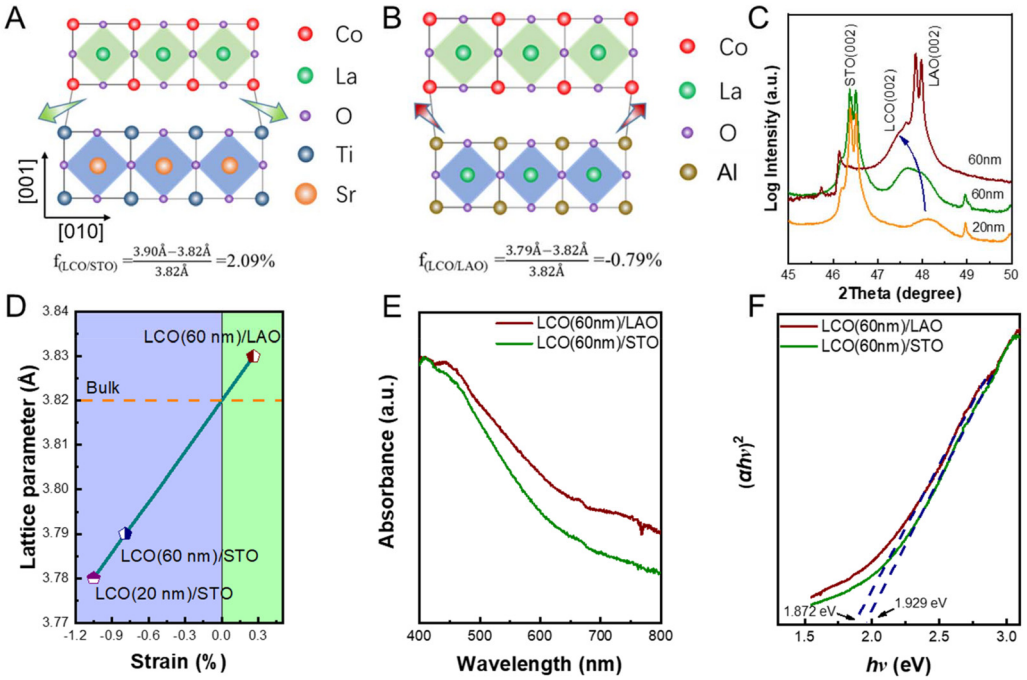

Fig. 1 Lattice analysis of LCO thin films on different substrates. (A) Schematic diagram of lattice matching for the LCO/STO structure. (B) Schematic diagram of lattice matching for the LCO/LAO structure. (C) XRD patterns with a small angle region of LCO (60 nm)/LAO, LCO (60 nm)/STO, and LCO (20 nm)/STO structures. (D) Variation of the out-of-plane lattice constant of LCO films with strain. (E) Optical absorption spectra of LCO (60 nm)/LAO and LCO (60 nm)/STO films. (F) Corresponding direct optical bandgap transitions for LCO (60 nm)/LAO and LCO (60 nm)/STO films.

compared to that of the 60 nm LCO films on STO substrates, indicating a larger out-of-plane lattice constant for LCO films on the LAO substrate with compressive strain along the in-plane direction. Additionally, the (002) diffraction peak of the 20 nm LCO films on STO substrates shifts to a higher angle relative to the 60 nm LCO films on the same substrates, demonstrating that thinner films are more susceptible to substrate strain (Fig. 1C). As shown in Fig. 1D, we further elucidate the relationship between the out-of-plane lattice constant and the out-of-plane strain degree. It shows that the compressive strain along the out-of-plane direction caused by the STO substrates decreases the *c*-axis lattice constant of the films, while the tensile strain caused by the LAO substrates increases it. This trend is consistent across the different film thicknesses, highlighting the significant influence of substrate strain on the lattice structure of LCO films. These results provide a fundamental understanding of how substrate strain can be utilized to engineer the properties of LCO films, offering a powerful tool for optimizing their performance in various applications.

Strain exerts significant effects on the crystal structure of LCO films, which in turn influences their electronic hybridization states considerably.[30,31] The variations in lattice parameters and alterations in atomic binding forces, both induced by substrate strain, can lead to shifts in band positions, thereby affecting the bandgap of LCO thin films. As depicted in Fig. 1E and F, the LCO films deposited on LAO substrates are subjected to the in-plane compressive strain, resulting in a decrease of the bandgap from ~1.93 eV for the films on STO substrates to ~1.87 eV. It is worth noting that the values of these bandgaps are lower than those reported for LCO measured through the same optical absorption spectra.[32,33] This is due to the lattice distortion caused by the substrate strain.[34] The change in bandgap not only demonstrates the role of strain in modulating the electronic properties of LCO films but also implies that substrate strain may have additional impacts on their stability. For instance, strain might result in local distortions in the crystal structure or the formation of defects. These factors can subsequently influence the chemical and physical properties of LCO films.

We further investigated the atomic structure of LCO films on different substrates using spherical aberration-corrected high-angle annular dark-field scanning transmission electron microscopy (HAADF-STEM). To ensure the accuracy of the STEM analysis, we deposited a platinum layer on the sample surface for protecting the films before using a focused ion beam to cut the samples. Fig. S3 shows the low-magnification HAADF-STEM images at the interface of LCO films and the substrates. The measurements reveal film thicknesses of ~20 nm, indicating that substrate strain does not affect the thickness of LCO films. The HAADF-STEM images at the interface clearly show the interface between the LCO films and the substrates (Fig. 2A and C). *The atomic*-level matching confirms the perovskite structure of LCO films, which is consistent with our earlier conclusions. We use *A* or *B* to represent the atomic positions in the oxide perovskite structure (ABO_3). The clear *A*

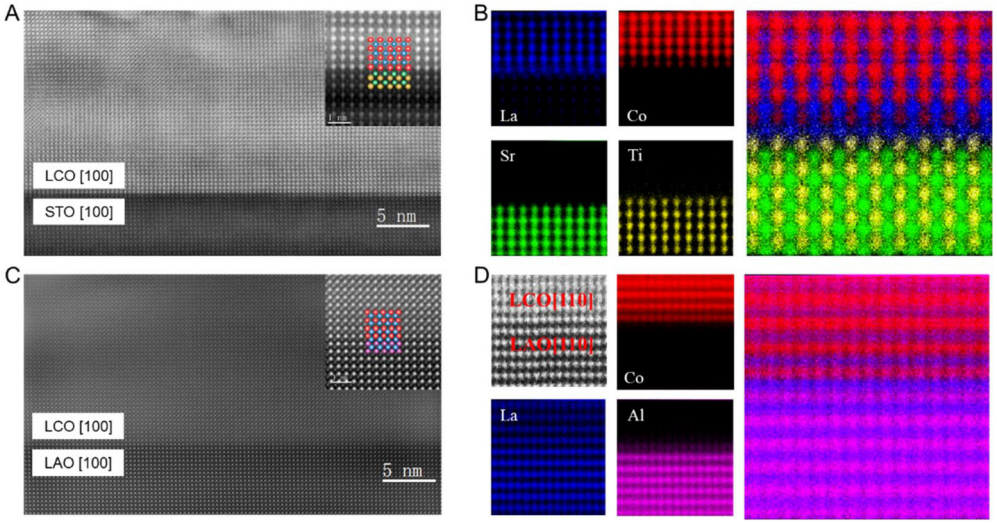

Fig. 2 Interface analysis of LCO films and the substrates. (A and C) Large-scale atomic-resolution HAADF-STEM images of LCO films along the substrates' [100] zone axis on STO (A) and LAO (C) substrates. The insets are the corresponding atomic arrangement schematics. (B) EDS maps of La, Co, Sr, and Ti elements and the corresponding map showing all elements. (D) Small-scale HAADF-STEM image of LAO along the [110] zone axis, EDS maps of La, Co, and Al elements, and the corresponding map showing all elements.

and *B*-site metal cation observation indicates the excellent crystallinity of LCO films. The original atomic arrangement at the interface also indicates the excellent epitaxial quality of the films compared to the substrates.

To further explore atomic ordering, energy-dispersive spectroscopy (EDS) analyses were performed at the interfaces of LCO/STO along the STO [100] zone axis and LCO/LAO along the LAO [110] zone axis (Fig. 2B and D). The EDS maps of LCO films on different substrates reveal a uniform and ordered elemental distribution (La, Co, Sr, Ti, and Al). Despite substrate-induced strain, the LCO films maintain good crystal structures and robust elemental distributions. At the LCO/STO interface, there is a distinct Ti element cutoff plane, and the La–O layer of LCO films and the Ti–O layer of STO substrates are mutually compatible, which may lead to charge transfer. In contrast, at the LCO/LAO interface, the Co–O layer of LCO films overlaps with the La–O layer of LAO substrates. This indicates that charge transfer is not expected to occur. These findings highlight the robustness of LCO films under different epitaxial conditions. This strain caused by the substrates is crucial for maintaining the electronic hybridization and structural distortion of the LCO films, and the detailed atomic-level insights provided by HAADF-STEM analysis further validate the effectiveness of our epitaxial growth process.

Additional HAADF-STEM tests were conducted on the LCO films on the two substrates to further demonstrate lattice distortion. Fig. 3 shows the small-scale HAADF-STEM images with the atomic-resolution microstructure (I) of LCO films on STO and LAO substrates along the substrates' [100] zone axis, the corresponding fast Fourier transform (FFT) images (insets in I), the corresponding inverse FFT images (II), and the corresponding geometric phase analysis (GPA) results (III and IV). The HAADF-STEM and FFT images indicate good crystal quality and show the pseudo-cubic structure of LCO films on both substrates (Fig. 3I). The inverse FFT images of LCO films on both substrates reveal the atomic intensity variations, enabling lattice constant calculation (Fig. 3II and S4). We selected over five interatomic spacings, keeping peak intensities on the same level to minimize errors. From the HAADF-STEM images along the [100] zone axis of the LCO films, it is found that the in-plane and out-of-plane lattice constants equal the vertical and parallel interatomic distances for the films. The results show that for the LCO films on STO substrates, the out-of-plane lattice constant of LCO films compresses by ~0.04 Å, the in-plane stretches by ~0.06 Å, and the unit-cell volume increases by ~1.85%. For the films on the LAO substrate, the out-of-plane lattice constant stretches by ~0.04 Å and the in-plane compresses by ~0.02 Å, and the unit-cell volume increases by ~0.29%. These changes indicate a strain effect of the substrate on the LCO films. The film strain caused by the substrate follows the Poisson deformation law. We also demonstrate this point through synchrotron-based X-ray reciprocal space mapping (RSM) patterns (Fig. S5). Along the in-plane direction, the diffraction peaks of LCO films grown on different substrates are close to those of their respective supporting substrates, respectively. Along the out-of-plane direction, compared to the original position, the diffraction peaks of the films are removed away from those of the substrate. This process of one axis being stretched and the other being compressed indicates the Poisson deformation that the LCO films undergo after being subjected to substrate strain on different substrates. The in-plane lattice constants of the LCO films do not exactly equal those of their respective supporting substrates, indicating the presence of strain relaxation. The LCO films on the STO substrates experience the out-of-plane compressive strain and in-plane tensile strain result-

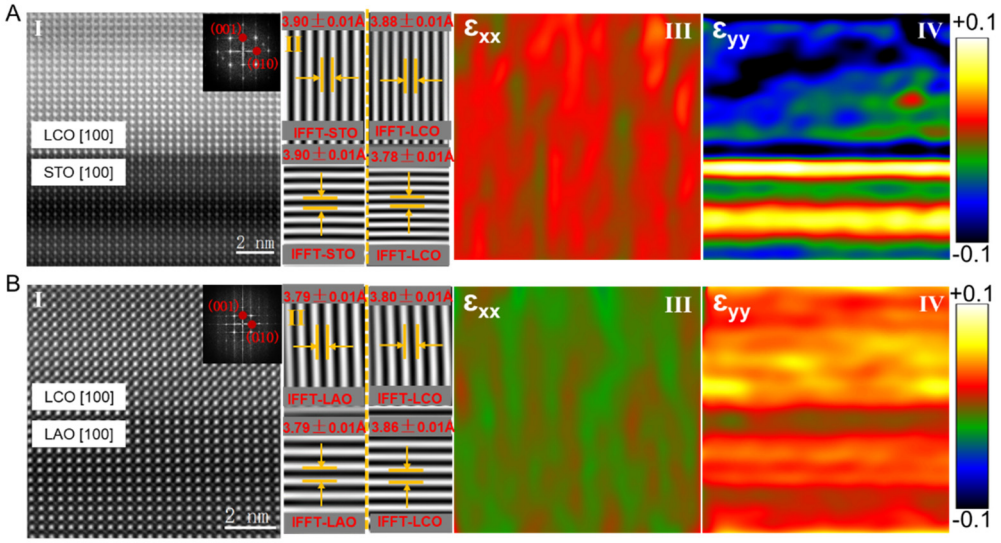

Fig. 3 Distortion analysis of LCO thin films on different substrates. (A and B) Small-scale atomic-resolution HAADF-STEM images (I), the corresponding inverse FFT images (II) and the corresponding GPA patterns (III and IV) for the interface regions of LCO thin films along the substrates' [100] zone axis on STO (A) and LAO substrates (B). The insets are the corresponding FFT images.

ing in smaller out-of-plane lattice constants. Conversely, the LCO films on the LAO substrates exhibit the out-of-plane tensile strain and in-plane compressive strain resulting in larger out-of-plane lattice constants. The out-of-plane and in-plane lattice constants of the films through the inverse FFT and RSM align with XRD results.

The GPA analysis further reveals the differences in strain distribution in LCO films on the two substrates, confirming the significant impact of substrate strain. The GPA results show that for the films on the STO substrates, the in-plane strain component ε_{xx} appears in red, indicating tensile strain (Fig. 3AIII), while the out-of-plane strain component ε_{yy} appears in blue, indicating compressive strain (Fig. 3AIV). In contrast, for the films on the LAO substrate, ε_{xx} appears in green, indicating compressive strain (Fig. 3BIII), while ε_{yy} appears in red, indicating tensile strain (Fig. 3BIV). This strain distribution highlights how the different substrates induce contrasting strain states in the LCO films, influencing their structural distortion and potentially their functional properties.

LCO is water-stable, which is different from SAO, indicating that it is highly stable under ambient air conditions. A thermodynamic analysis using HSC Chemistry 9 software reveals that LCO perovskites exhibit a spontaneous chemical reaction with hydrogen ions, which is evidenced by the negative Gibbs free energy of −1350.6 kJ for $LaCoO_3 + 6H^+ \rightarrow La^{3+} + Co^{3+} + H_2O$.[35] Our experiments also show that LCO films can be decomposed by weak acids (CH_3COOH) during the soaking process, which is consistent with the thermodynamic results. In order to evaluate the decomposition rate of LCO films in CH_3COOH, we conducted semi-*in situ* tests using ultraviolet–visible (UV-Vis) optical absorption spectra. It measures the changes in the optical absorption coefficient (α) within the UV-Vis light range to investigate the decomposition extent of films. In this experiment, tracking the decomposition process by monitoring changes in the α of LCO films in 10% CH_3COOH solution in real time proved effective. Additionally, to more intuitively observe the film decomposition, optical photographs are employed to record morphological changes during processing. Combined with optical data, these images helped confirm the decomposition behavior.

Fig. 4A and B display the optical absorption spectra of LCO thin films with ~60 nm thickness grown on LAO and STO substrates after soaking in 10% CH_3COOH solution for different durations. The α values of LCO films on both substrates decrease over time, indicating the decomposition of the LCO films. The results indicate that the decomposition rate correlates with the change in the α of the absorption edge. The LCO films on STO substrates show a faster α decline, suggesting a higher decomposition rate than that for films on LAO substrates. The α at a wavelength of 400 nm decays from an initial value of around 0.4 to near 0.05. For the LCO films on LAO substrates, this process takes close to 60 hours, whereas for the LCO films on STO substrates, it takes only 36 hours. This represents an approximately 67% increase in the decomposition rate for the LCO films on STO substrates compared to the films on LAO substrates. Fig. 4C displays the optical photographs of LCO films on the different substrates under the same soaking conditions. Over time, the color of the films gradually fades from brown to the color of the double-polished substrate itself. The substrates not being transparent is due to the rearrangement of oxygen vacancies in the annealing process. The standardized optical absorption spectra of LCO films on STO substrates indicate that the slight errors introduced by substrate annealing do not lead to incorrect judgments of the decomposition time of LCO (Fig. S6). The LCO

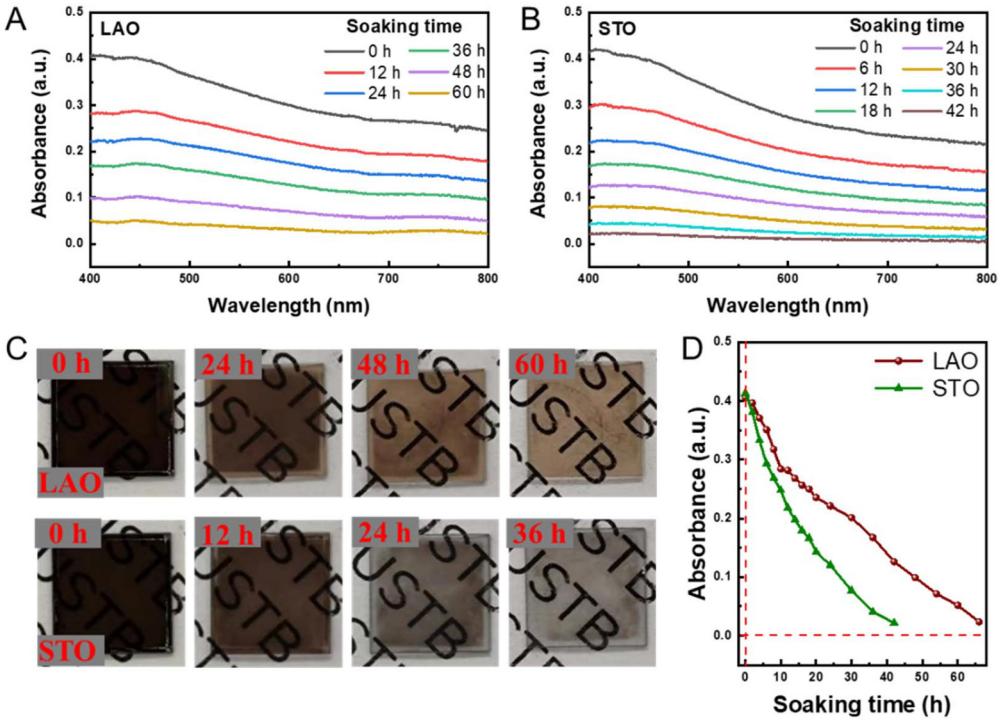

Fig. 4 Decomposition process of LCO thin films with 60 nm thickness soaked in 10% CH_3COOH solution. (A and B) Optical absorption spectra of LCO films on LAO (A) and STO (B) substrates at different times. (C) Optical photographs of LCO films on LAO and STO substrates (10 × 10 mm^2) at different times. (D) Curves of absorbance (λ = 400 nm) variation of LCO films on the two substrates with soaking time.

films on STO substrates achieve complete decomposition in only 36 hours, while those on LAO substrates require 60 hours. This finding is consistent with the results of optical absorption spectra and confirms that the LCO films on STO substrates undergo faster decomposition.

Fig. 4D displays the relationship between the absorbance at 400 nm and the soaking time. At the beginning of the soaking process, the initial decline rates of absorbance for LCO films on both STO and LAO substrates are comparable. However, as the soaking time increases, the decline rate for the LCO films on STO substrates became more pronounced than that for the films on LAO substrates. This observed difference can be attributed to the varying degrees of substrate strain experienced by the thin films during the reaction process. In the early soaking stage, the surfaces of the LCO films on both STO and LAO substrates are subjected to relatively low levels of substrate strain, resulting in similar decomposition rates. As the reaction progresses and extends deeper into the film interiors, the greater substrate strain has a more significant impact on the structural integrity and chemical stability for the LCO films on STO substrates. Consequently, this leads to a faster decomposition rate of the LCO films on STO substrates compared to those on LAO substrates. To further investigate this phenomenon, experiments are conducted in which the LCO films with ~20 nm thickness are soaked in 10% CH_3COOH solution (Fig. S7A and S7B). The absorbance of LCO films on both LAO and STO substrates decreases with soaking time, indicating that the films undergo decomposition in acetic acid solution. Notably, compared to the 60 nm thick films, the 20 nm thick films exhibited significant initial absorbance differences (Fig. S7C). The absorbance of LCO films on STO substrates consistently declined more rapidly than that of films on LAO substrates. This indicates that the chemical decomposition of LCO films on STO substrates occurs at a faster rate, which can be attributed to the influence of lattice strain on chemical stability and decomposition kinetics of the films.

X-ray absorption spectroscopy (XAS) was implemented to confirm the lattice distortion and Co–O octahedral orbital hybridization in LCO perovskite films on different substrates. Fig. 5A displays the normalized XAS spectra of Co *L*-edge and the difference curves for LCO perovskite films on different substrates. The Co L_3 regions of the films are split into e_g and t_{2g} peaks, with significant differences between them (the top in Fig. 5A). To analyze the differences between the films on the two different substrates, the Co L_3-edge XAS spectra of the two films are normalized to the peak of maximum intensity, and then subtracted to obtain the difference curves (the bottom in Fig. 5A). The difference curves show the alternating changes in intensity (increase first and then decrease, then increase and decrease), indicating the energy level splitting of the LCO films on LAO substrates compared with those on STO substrates. This means that compared with the films on STO substrates, the out-of-plane axis in Co–O octahedra of the films on the

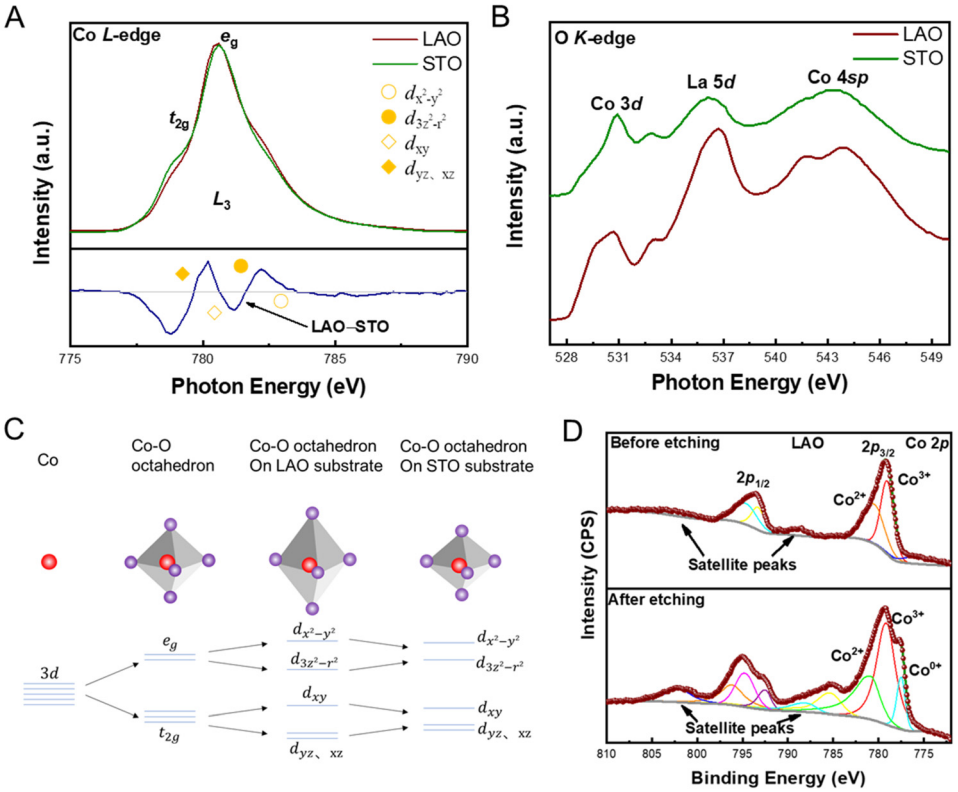

Fig. 5 XAS and XPS spectral analysis of LCO thin films on different substrates. (A) Normalized Co *L*-edge XAS spectra (top) and difference curves (bottom) of LCO thin films on different substrates. (B) O *K*-edge XAS spectra of LCO thin films on different substrates. (C) Schematic diagrams of local structures and orbital changes for Co–O octahedra on different substrates. (D) Co 2p XPS spectra of LCO thin films on the LAO substrate before and after Ar^+ etching.

LAO substrates is longer, with the Co–O bond being stretched in the out-of-plane direction but shortened in the in-plane direction, while the corresponding La–O bond is also shortened in the in-plane direction. We compared the O *K*-edge XAS spectra of LCO films on different substrates to further verify the distortion of the Co–O octahedra (Fig. 5B). The O *K*-edge XAS spectra of LCO films can be divided into orbital characteristic regions of Co 3d, La 5d, and Co 4sp. Compared with the films on STO substrates, the obvious splitting of the Co 3d and Co 4sp peaks proves the significant octahedral distortion of the Co–O octahedra for the films on the LAO substrates. Since XAS intensity represents the density of unoccupied orbital states in films,[34,36] the intensity of the La 5d peak of the films on LAO substrates is higher than that of the films on STO substrates, further confirming that the La–O bond is compressed along the in-plane direction. It should be noted that the distortion of the Co–O octahedra should result from the different lattice matching modes between the film and the substrate.

To better comprehend the octahedral distortion in LCO films on different substrates, this study employs crystal field theory to illustrate the local structure and orbital variations of Co–O octahedra with distinct symmetries (Fig. 5C).[37] It corresponds one-to-one with the difference curves, which proves the Jahn–Teller distortion caused by the substrate strain. In spherical symmetry, the Co 3d energy level comprises five degenerate orbitals with the same energy. In the Co–O octahedral symmetry, the Co 3d level splits into e_g and t_{2g} levels, with the energy of $e_g > t_{2g}$. Within the Co–O octahedra of the LCO perovskite films, the e_g level undergoes further splitting into $d_{x^2-y^2}$ (○) and $d_{3z^2-r^2}$ (●) orbitals, while the t_{2g} level splits into d_{xy} (◊), d_{yz} (◆), and d_{xz} (◆) orbitals, with the latter two exhibiting the same energy. As for the Co–O octahedra of LCO films on LAO substrates, the symmetry reduction is attributed to elongation along the *c*-axis, which gives rise to an orbital energy distribution of $d_{x^2-y^2} > d_{3z^2-r^2} > d_{xy} > d_{yz,\ xz}$. The Co–O octahedra in the films on STO substrates shorten along the *c*-axis due to compressive strain along the out-of-plane direction. This phenomenon causes a reduction in the out-of-plane lattice constant of the films, which is in accordance with XRD results. The previous study has determined that the separation of La atoms is an important link in the decomposition process of La-based films in acetic acid.[38] The XAS analysis indicates that for LCO films on LAO substrates, stretching of Co–O bonds happens along the out-of-plane direction. As the LCO films follow the Poisson deformation law, La–O bonds are compressed along the in-plane direction. This elevates bond energy, thus impeding La atom detachment. Conversely, the

Co–O bonds in the LCO films on STO substrates are compressed along the out-of-plane direction, inducing stretching of La–O bonds along the in-plane direction. This reduces bond energy and promotes La atom detachment. These findings are consistent with the above results from the optical absorption spectra, highlighting the significant impact of lattice strain on LCO thin film decomposition in acetic acid.

X-ray photoelectron spectroscopy (XPS) was employed to analyze the elemental composition of the LCO films on different substrates. The XPS full spectra of the LCO films on different substrates show the characteristic peaks of Co 2p, La 3d, and O 1s (Fig. S8). These peaks confirm the presence of Co, La, and O elements in the films. Fig. 5D presents the XPS spectra of Co 2p of the LCO films on LAO substrates before and after Ar^+ ion etching. The Co 2p XPS spectra show Co characteristic peaks, including Co $2p_{3/2}$ and Co $2p_{1/2}$. Fitting deconvoluted the Co 2p spectra into three parts: Co^{2+}, Co^{3+}, and their corresponding satellite peaks. Before Ar^+ etching, the LCO films exhibit Co^{2+}, Co^{3+}, and their corresponding satellite peaks. After Ar^+ etching, a Co^{0+} characteristic peak appears at a binding energy of approximately 777.5 eV, while the intensity of the Co^{3+} characteristic peak at around 779.0 eV decreases, indicating that Co^{3+} is reduced during etching. This phenomenon has also been observed in the Fe XPS spectra of the $LiFePO_4$ electrode.[39] Note that the comparison reveals that Co^{0+} peaks in LCO films on LAO substrates are higher than those on STO substrates (Fig. S9). This implies that Co elements are easily reduced in LCO films on LAO substrates. This suggests that Co–O bonds in LCO films on LAO substrates have lower bond energy compared to those in the films on STO substrates, consistent with previous XAS analysis.

Given the decomposition properties of LCO films, it is viable to prepare freestanding films using LCO as a sacrificial layer. We selected $PbZrO_3$ (PZO), a classic antiferroelectric material with a perovskite structure and a lattice constant of about 4.21 Å, for stripping to demonstrate the lattice compatibility of the LCO sacrificial layer. The directional electrodynamic decomposition, a technique reported in our prior work, is used to accelerate the decomposition process to ensure the flatness and integrity of freestanding films (Fig. S10).[38] Fig. S11 shows the XRD pattern of PZO and LCO films grown on the (001) STO substrates. The diffraction peaks of STO (00L), LCO (00L) and PZO (00L) are clear, indicating that the (001) plane of the films grows parallel to the substrate (001) plane and showing a good epitaxial relationship and high-orientation of the films. After LCO decomposition, the peaks of the PZO film (00L) remain strong, while those of STO and LCO disappear, confirming that the PZO film is successfully stripped from the STO substrate. The positions of the XRD diffraction peaks of the stripped PZO films shift slightly towards larger angles, indicating a slight release of strain. Fig. S12A shows macro- and microimages of the freestanding PZO films. The dimension is about 5×3 mm^2 for the freestanding PZO films. The freestanding PZO films have a high integrity after the stripping process. This suggests that during the decomposition of the LCO sacrificial layer, the atomic mismatch strains did not significantly spread to the freestanding films. Despite some minor surface impurities likely from airborne contaminants during preparation, the overall structure of the films remains intact. An atomic force microscope (AFM) was used to characterize the surface morphology of freestanding PZO films. Fig. S12B shows the AFM surface morphology of freestanding PZO films of a 10 $\times$ 10 μm^2 scale. The local measurements from the area of the sample reveal a fine and uniform grain distribution with high surface flatness and no obvious uneven areas or significant height differences. The average roughness of the films is only about 1 nm. To better understand the roughness distribution of the films, a line is randomly drawn in Fig. S12B. It can be observed that the amplitudes are distributed within the range of ±300 pm (Fig. S12C), which shows that the film surface has good uniformity.

Many studies have shown that PZO can transform from an antiferroelectric to a ferroelectric state under strain changes.[40] We used piezoresponse force microscopy (PFM) to investigate the ferroelectric properties of freestanding PZO films. The cantilever probe applies a voltage over an area of 5×5 μm^2 (−10 V in the outer square and +10 V in the inner square). The amplitude image shows a clear "box-in-box" piezoelectric response of the surface of freestanding films (Fig. S13A). The phase image reveals a distinct "box-in-box" domain switching (Fig. S13B), with good correspondence between the local amplitude and the phase switching. This confirms that the freestanding PZO films undergo a strain-induced antiferroelectric-to-ferroelectric transition after stripping. On the STO substrates, the PZO thin films undergo tensile strain and tend towards antiferroelectricity.[41] This strain release will cause them to undergo a transition to the orthorhombic ferroelectric-like phase. This phase transition will not result in any change to the lattice structure (space group remains *Pbam*), but only involves a change in the reverse displacement of the atoms from "↑↑↓↓" to "↑↑↓".[42] This phenomenon indicates the effectiveness of the freestanding PZO films during its application process.

Conclusion

In summary, this study has thoroughly examined how substrate strain impacts the structural and decomposition properties of LCO films. Our findings reveal that LCO films undergo distinct decomposition rate variations when subjected to different substrate strains. These variations are primarily attributed to the alterations in the lattice structure and chemical bonding of LCO films induced by strain. Through meticulous analysis employing XRD, STEM, XAS, and XPS, we have gained profound insights into the mechanisms underlying these strain-induced effects on LCO films. The strain modulation has proven to be a powerful tool for influencing the decomposition behavior of LCO thin films. The LCO films under compressive strain on STO substrates exhibit a faster decomposition rate than those under tensile strain on LAO substrates. This discrepancy stems from substrate strain-induced variations in the La–O bond. Stretched La–O

bonds in the films on STO substrates reduce bond energy and facilitate La atom detachment, thereby accelerating decomposition, while compressed La–O bonds in the films on LAO increase bond energy and hinder La atom release. These results deepen the understanding of the fundamental properties of LCO films and offer a novel strategy for regulating sacrificial layer decomposition in film device fabrication. Modulating LCO film decomposition *via* strain engineering unlocks new application prospects, especially for flexible electronic devices that require precise control over material removal and transfer processes.

Author contributions

Jie Tu, Siyuan Du, and Hangren Li contributed equally to this work. Siyuan Du, Jie Tu, Hangren Li, and Linxing Zhang conceived the idea. Siyuan Du fabricated the films with the help of Jie Tu and Hangren Li. Siyuan Du carried out the stripping of freestanding films with the help of Hangren Li and Jie Tu. Siyuan Du, Hangren Li, and Linxing Zhang performed and analyzed optical characterization. Jie Tu and Hangren Li performed ferroelectric characterization. Jie Tu, Siyuan Du, Hangren Li, and Longyuan Shi conducted and analyzed structural characterization (XRD and RSM). Jie Tu, Siyuan Du, Hangren Li, Longyuan Shi, Jianjun Tian, and Linxing Zhang analyzed other data. Jing Xia performed the STEM characterization. Jie Tu and Siyuan Du wrote the manuscript with contributions from others. All authors were involved in the data analyses and commented on the manuscript. Jie Tu revised the manuscript with contributions from others. Jianjun Tian and Linxing Zhang supervised the project.

Conflicts of interest

The authors declare no competing financial interests.

Data availability

The data that support the findings of this study are available from the corresponding author upon reasonable request.

Supplementary information (SI) is available. The SI section included more detailed experimental procedures, as well as lattice analysis (XRD, rocking curves, HAADF-STEM, RSM) of LCO films under different strain conditions, decomposition efficiency of LCO films with varying thicknesses, supplementary XPS spectra, and characterization and performance results of freestanding PZO films. See DOI: **https://doi.org/10.1039/d5qi01871d**.

Acknowledgements

This work was supported by the National Key Research and Development Program of China (2025YFA1411900 and 2021YFF0704705), the National Natural Science Foundation of China (22371013 and 92263205), the Fundamental Research Funds for the Central Universities (FRF-TP-19-055A2Z), the National Program for Support of Top-notch Young Professionals, and the Young Elite Scientists Sponsorship Program by CAST (2019-2021QNRC), the "Xiaomi Young Scholar" Funding Project, Scientific Equipment Development Project of Chinese Academy of Sciences, Youth Innovation Promotion Association Project of Chinese Academy of Sciences (2020026), and the Technical Support Talent Project of Chinese Academy of Sciences. We thank the 4B9B Beamline of Beijing Synchrotron Radiation Facility (**https://cstr.cn/31109.02.BSRF.4B9B**) for providing technical support and assistance in XAS data collection and the 1 W1A Beamline of Beijing Synchrotron Radiation Facility (**https://cstr.cn/31109.02.BSRF.1W1A**) for providing technical support and assistance in structural data collection.

References

1 T. Q. Trung and N.-E. Lee, Flexible and stretchable physical sensor integrated platforms for wearable human-activity monitoringand personal healthcare, *Adv. Mater.*, 2016, **28**(22), 4338–4372.
2 D.-H. Kim, N. Lu, R. Ma, Y.-S. Kim, R.-H. Kim, S. Wang, J. Wu, S. M. Won, H. Tao, A. Islam, K. J. Yu, T.-i. Kim, R. Chowdhury, M. Ying, L. Xu, M. Li, H.-J. Chung, H. Keum, M. McCormick, P. Liu, Y.-W. Zhang, F. G. Omenetto, Y. Huang, T. Coleman and J. A. Rogers, Epidermal electronics, *Science*, 2011, **333**(6044), 838–843.
3 D. Lu, D. J. Baek, S. S. Hong, L. F. Kourkoutis, Y. Hikita and H. Y. Hwang, Synthesis of freestanding single-crystal perovskite films and heterostructures by etching of sacrificial water-soluble layers, *Nat. Mater.*, 2016, **15**(12), 1255–1260.
4 T. Detchprohm, H. Amano, K. Hiramatsu and I. Akasaki, The growth of thick GaN film on sapphire substrate by using ZnO buffer layer, *J. Cryst. Growth*, 1993, **128**(1–4), 384–390.
5 D. M. Paskiewicz, R. Sichel-Tissot, E. Karapetrova, L. Stan and D. D. Fong, Single-crystalline $SrRuO_3$ nanomembranes: a platform for flexible oxide electronics, *Nano Lett.*, 2016, **16**(1), 534–542.
6 S. R. Bakaul, C. R. Serrao, M. Lee, C. W. Yeung, A. Sarker, S.-L. Hsu, A. K. Yadav, L. Dedon, L. You, A. I. Khan, J. D. Clarkson, C. Hu, R. Ramesh and S. Salahuddin, Single crystal functional oxides on silicon, *Nat. Commun.*, 2016, **7**(1), 10547.
7 Y.-W. Chang, P.-C. Wu, J.-B. Yi, Y.-C. Liu, Y. Chou, Y.-C. Chou and J.-C. Yang, A fast route towards freestanding single-crystalline oxide thin films by using $YBa_2Cu_3O_{7-x}$ as a sacrificial layer, *Nanoscale Res. Lett.*, 2020, **15**(1), 172.
8 K. Eom, M. Yu, J. Seo, D. Yang, H. Lee, J.-W. Lee, P. Irvin, S. H. Oh, J. Levy and C.-B. Eom, Electronically reconfigurable complex oxide heterostructure freestanding membranes, *Sci. Adv.*, 2021, **7**(33), eabh1284.

9 H. Peng, N. Lu, S. Yang, Y. Lyu, Z. Liu, Y. Bu, S. Shen, M. Li, Z. Li, L. Gao, S. Lu, M. Wang, H. Cao, H. Zhou, P. Gao, H. Chen and P. Yu, A generic sacrificial layer for wide-range freestanding oxides with modulated magnetic anisotropy, *Adv. Funct. Mater.*, 2022, **32**(28), 2111907.
10 Y. Bourlier, B. Bérini, M. Frégnaux, A. Fouchet, D. Aureau and Y. Dumont, Transfer of epitaxial $SrTiO_3$ nanothick layers using water-soluble sacrificial perovskite oxides, *ACS Appl. Mater. Interfaces*, 2020, **12**(7), 8466–8474.
11 J. Zhang, T. Lin, A. Wang, X. Wang, Q. He, H. Ye, J. Lu, Q. Wang, Z. Liang, F. Jin, S. Chen, M. Fan, E.-J. Guo, Q. Zhang, L. Gu, Z. Luo, L. Si, W. Wu and L. Wang, Super-tetragonal $Sr_4Al_2O_7$ as a sacrificial layer for high-integrity freestanding oxide membranes, *Science*, 2024, **383**(6681), 388–394.
12 P.-W. Shao and Y.-H. Chu, Advances in strain engineering on oxide heteroepitaxy, *Matter*, 2021, **4**(7), 2117–2119.
13 J. Tu, D. Zheng, X. Liu, H. Li, Y. Wu, S. Du, J. Ding, X. Liu, M. Li, Q. Wang, X. Shi, X. Zhang, J. Tian and L. Zhang, Atomical-rippled-nanodomains stabilized large polarization in $BiSmCo_2O_6$ double-perovskite films, *Adv. Mater.*, 2025, e09635.
14 H. Li, J. Tu, J. Ding, J. Xia, L. Shi, S. Du, X. Liu, X. Liu, M. Li, J. Tian and L. Zhang, Ultrahigh remanent polarization of Ce-doped HfO_2 ferroelectric thin film through strain engineering, *Sci. China Mater.*, 2025, **68**, 2792–2798.
15 L. Sementilli, E. Romero and W. P. Bowen, Nanomechanical dissipation and strain engineering, *Adv. Funct. Mater.*, 2022, **32**(3), 2105247.
16 Y. Miao, Y. Zhao, S. Zhang, R. Shi and T. Zhang, Strain engineering: a boosting strategy for photocatalysis, *Adv. Mater.*, 2022, **34**(29), 2200868.
17 M. Li, J. Zheng, X. Wang, R. Yu, Y. Wang, Y. Qiu, X. Cheng, G. Wang, G. Chen, K. Xie and J. Tang, Light-responsive self-strained organic semiconductor for large flexible OFET sensing array, *Nat. Commun.*, 2022, **13**(1), 4912.
18 H. Cheng, P. Jiao, J. Wang, M. Qing, Y. Deng, J.-M. Liu, L. Bellaiche, D. Wu and Y. Yang, Tunable and parabolic piezoelectricity in hafnia under epitaxial strain, *Nat. Commun.*, 2024, **15**(1), 394.
19 S. J. Yoo, J. Hwang, J. Jang, J. H. Jang, C. H. Park, J.-H. Lee, M. Y. Choi, J. M. Yuk, S.-Y. Choi, J. Lee and S.-Y. Chung, Comparing the impacts of strain types on oxygen-vacancy formation in a perovskite oxide via nanometer-scale strain fields, *ACS Nano*, 2024, **18**(28), 18465–18476.
20 Q. Zhang, F. Meng, A. Gao, X. Li, Q. Jin, S. Lin, S. Chen, T. Shang, X. Zhang, H. Guo, C. Wang, K. Jin, X. Wang, D. Su, L. Gu and E.-J. Guo, Dynamics of anisotropic oxygen-ion migration in strained cobaltite, *Nano Lett.*, 2021, **21**(24), 10507–10515.
21 S. Yoon, X. Gao, J. M. Ok, Z. Liao, M.-G. Han, Y. Zhu, P. Ganesh, M. F. Chisholm, W. S. Choi and H. N. Lee, Strain-induced atomic-scale building blocks for ferromagnetism in epitaxial $LaCoO_3$, *Nano Lett.*, 2021, **21**(9), 4006–4012.
22 Q. Zhang, A. Gao, F. Meng, Q. Jin, S. Lin, X. Wang, D. Xiao, C. Wang, K.-j. Jin, D. Su, E.-J. Guo and L. Gu, Near-room temperature ferromagnetic insulating state in highly distorted $LaCoO_{2.5}$ with CoO_5 square pyramids, *Nat. Commun.*, 2021, **12**(1), 1853.
23 D. Li, H. Wang, K. Li, B. Zhu, K. Jiang, D. Backes, L. S. I. Veiga, J. Shi, P. Roy, M. Xiao, A. Chen, Q. Jia, T.-L. Lee, S. S. Dhesi, D. O. Scanlon, J. L. MacManus-Driscoll, P. A. van Aken, K. H. L. Zhang and W. Li, Emergent and robust ferromagnetic-insulating state in highly strained ferroelastic $LaCoO_3$ thin films, *Nat. Commun.*, 2023, **14**(1), 3638.
24 S. Chen, J.-Y. Chang, Q. Zhang, Q. Li, T. Lin, F. Meng, H. Huang, Y. Si, S. Zeng, X. Yin, M. N. Duong, Y. Lu, L. Chen, E.-J. Guo, H. Chen, C.-F. Chang, C.-Y. Kuo and Z. Chen, Spin state disproportionation in insulating ferromagnetic $LaCoO_3$ epitaxial thin films, *Adv. Sci.*, 2023, **10**(27), 2303630.
25 W. S. Choi, J.-H. Kwon, H. Jeen, J. E. Hamann-Borrero, A. Radi, S. Macke, R. Sutarto, F. He, G. A. Sawatzky, V. Hinkov, M. Kim and H. N. Lee, Strain-induced spin states in atomically ordered cobaltites, *Nano Lett.*, 2012, **12**(9), 4966–4970.
26 D. Shin, S. Yoon, S. Song, S. Park, H. N. Lee and W. S. Choi, Tunable ferromagnetism in $LaCoO_3$ epitaxial thin films, *Adv. Mater. Interfaces*, 2022, **9**(20), 2200433.
27 J. Wang, J. B. Neaton, H. Zheng, V. Nagarajan, S. B. Ogale, B. Liu, D. Viehland, V. Vaithyanathan, D. G. Schlom, U. V. Waghmare, N. A. Spaldin, K. M. Rabe, M. Wuttig and R. Ramesh, Epitaxial $BiFeO_3$ multiferroic thin film heterostructures, *Science*, 2003, **299**(5613), 1719–1722.
28 H. Li, Y. Yang, S. Deng, L. Zhang, S. Cheng, E.-J. Guo, T. Zhu, H. Wang, J. Wang, M. Wu, P. Gao, H. Xiang, X. Xing and J. Chen, Role of oxygen vacancies in colossal polarization in $SmFeO_{3-\delta}$ thin films, *Sci. Adv.*, 2022, **8**(13), eabm8550.
29 D. Chen, X. Tan, Y. Zhang and J. Jiang, The observation of polarization fatigue in epitaxial $BiFeO_3$ thin films with inhibited ferroelastic switching, *ACS Appl. Mater. Interfaces*, 2025, **17**(15), 22974–22983.
30 J. Tu, H. Li, X. Liu, G. Xi, X. Liu, M. Zhang, R. Wu, S. Du, D. Lu, L. Shi, J. Xia, Y.-W. Fang, J. Ding, Y. Liu, Y. Jia, M. Yuan, R. Yang, X. Li, X. Meng, J. Tian, L. Zhang and X. Xing, Giant switchable ferroelectric photovoltage in double-perovskite epitaxial films through chemical negative strain, *Sci. Adv.*, 2025, **11**(17), eads4925.
31 J. Tu, Y.-W. Fang, Y. Lu, H. Li, G. Xi, J. Ding, X. Liu, X. Liu, Q. Yang, J. Tian and L. Zhang, Strain-controlled oxygen vacancy for robust ferroelectric $BiSmFe_2O_{6-\delta}$ double-perovskite epitaxial thin films, *Appl. Phys. Rev.*, 2024, **11**(1), 011413.
32 P. Tiwari, A. D. Singha, S. A. Atkar, A. Datta and S. Thota, Probing the incoherent admixture of low and high-spin states of Co in $(LaPr)CoO_3$ perovskite: focus on structural phase transitions, *J. Phys.:Condens. Matter*, 2023, **35**, 375402.
33 D. A. Alshammari, Synthesis of Ag and Gd co-doped $LaCoO_3$: Tuning the optical bandgap through quantum

confinement effect for outstanding photocatalytic activity, *Ceram. Interfaces*, 2025, **51**(3), 3595–3606.

34 J. Tu, J. Ding, G. Xi, H. Li, Q. Yang, J. Tian and L. Zhang, Controllable chemical composition in double-perovskite $Bi_{0.5}Sm_{0.5}FeO_3$ epitaxial thin films for ferroelectric, photovoltaic, and ferromagnetic properties, *Chem. Eng. J.*, 2023, **453**, 139726.

35 B.-C. Lee, S.-B. Kim, J.-K. Moon and S.-Y. Park, Evaluation of reaction spontaneity for acidic and reductive dissolutions of corrosion metal oxides using HyBRID chemical decontamination, *J. Radioanal. Nucl. Chem.*, 2020, **323**, 91–103.

36 A. Ablat, R. Wu, M. Mamat, J. Li, E. Muhemmed, C. Si, R. Wu, J. Wang, H. Qian and K. Ibrahim, Structural analysis and magnetic properties of Gd doped $BiFeO_3$ ceramics, *Ceram. Int.*, 2014, **40**(9), 14083–14089.

37 K.-T. Ko, M. H. Jung, Q. He, J. H. Lee, C. S. Woo, K. Chu, J. Seidel, B.-G. Jeon, Y. S. Oh, K. H. Kim, W.-I. Liang, H.-J. Chen, Y.-H. Chu, Y. H. Jeong, R. Ramesh, J.-H. Park and C.-H. Yang, Concurrent transition of ferroelectric and magnetic ordering near room temperature, *Nat. Commun.*, 2011, **2**(1), 567.

38 H. Li, J. Tu, S. Du, G. Xi, C. Liu, Y.-W. Fang, S. Xu, J.-H. Zhang, E. Sun, S. Ouyang, X. Liu, L. Shi, X. Liu, D. Zheng, L. Guo, X. Zhang, K. Jin, J. Tian, L. Zhang and X. Xing, Efficient electrodynamic stripping for 12-inch wafer-scale freestanding ferroelectric membranes, *PREPRINT Research Square*, 2025, DOI: **10.21203/rs.3.rs-6397992/v1**.

39 X.-X. Zhao, X.-T. Wang, J.-Z. Guo, Z.-Y. Gu, J.-M. Cao, J.-L. Yang, F.-Q. Lu, J.-P. Zhang and X.-L. Wu, Dynamic Li^+ capture through ligand–chain interaction for the regeneration of depleted $LiFePO_4$ cathode, *Adv. Mater.*, 2024, **36**(14), 2308927.

40 Z. Yu, N. Fan, Z. Fu, B. He, S. Yan, H. Cai, X. Chen, L. Zhang, Y. Zhang, B. Xu, G. Wang and F. Xu, Room-temperature stabilizing strongly competing ferrielectric and antiferroelectric phases in $PbZrO_3$ by strain-mediated phase separation, *Nat. Commun.*, 2024, **15**(1), 3438.

41 S. E. Reyes-Lillo and K. M. Rabe, Antiferroelectricity and ferroelectricity in epitaxially strained $PbZrO_3$ from first principles, *Phys. Rev. B: Condens. Matter Mater. Phys.*, 2013, **88**(18), 180102.

42 Y. Liu, R. Niu, R. Uriach, D. Pesquera, J. M. C. Roque, J. Santiso, J. M. Cairney, X. Liao and J. Arbiol, G Catalan, Coexistence of ferroelectric and ferrielectric phases in ultrathin antiferroelectric $PbZrO_3$ thin films, *Microstructures*, 2024, **4**, 2024045.